ACS OMEGA

http://pubs.acs.org/journal/acsodf

Article

Ni-Containing Electrolytes for Superior Zinc-Ion Aqueous Batteries with Zinc Hexacyanoferrate Cathodes

Ratul Rehman,[‖] Xiaolin Zhang,[‖] Miao Chang, Daomin Qin, Yi Liu, Peng Wei, Chao Huang, Bin Wang, Fangyu Xiong, Yue Xu,* Pei Hu,* Jiantao Han, and Paul K. Chu

Cite This: *ACS Omega* 2022, 7, 33942−33948

Read Online

ACCESS | Metrics & More | Article Recommendations | Supporting Information

ABSTRACT: A one-step coprecipitation process is designed to synthesize zinc hexacyanoferrate (ZnHCF) cathodes in aqueous zinc-ion batteries (ZIBs). The morphology of the cathode is influenced by the concentration of the precursor solution and valence of iron ions. The rhombohedral ZnHCF sample exhibits high crystallinity on the microscale in the cut-angle cubic structure, whereas Na-rich NaZnHCF contains many interstitial water molecules in the rhombic nanoplates. Both samples show effective insertion of Zn ions in the aqueous $ZnSO_4$ solution. ZnHCF shows a specific capacity of 66.7 mA h g^{-1}, a redox voltage of 1.73 V, and fast decline in a few cycles. On the other hand, NaZnHCF has a lower specific capacity of 48.2 mA h g^{-1}, showing two voltage platforms and robust cycling stability. However, owing to serious side reactions, both samples have low Columbic efficiency. To improve the properties such as Coulombic efficiency, specific capacity, and cycling stability, Ni ions are introduced by adding 10 wt % $NiSO_4$ to the $ZnSO_4$ electrolyte. The ZnHCF cathode in the Ni-containing electrolyte has the best properties such as a high specific capacity of 71.2 mA h g^{-1} at a current density of 100 mA g^{-1}, 93% retention of the Coulombic efficiency, and a good rate performance manifested by a reversible capacity of 58.2 mA h g^{-1} at 1 A g^{-1}. The results reveal a strategy to improve the electrochemical properties of aqueous ZIBs by modifying the electrolytes.

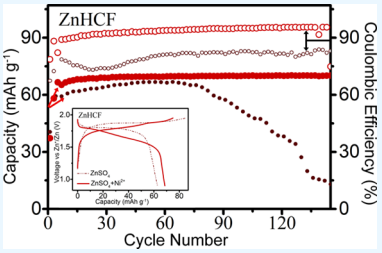

1. INTRODUCTION

Aqueous rechargeable batteries with low production costs, nonflammability, environmental friendliness, operating safety, and high ion mobility are desirable for grid-scale energy storage.[1,2] Aqueous rechargeable Zn-ion batteries (ZIBs) have evolved as a new energy storage system that is expected to provide a new option for large-scale energy storage.[3] Zinc is abundant on earth and relatively economical, and the corresponding inorganic salts are nontoxic.[4] Aqueous ZIBs operate by two-electron transfer *via* transportation of divalent zinc ions to provide a high energy density and fast charging.[5] However, owing to slow Zn^{2+} diffusion in the host, reversible intercalation/deintercalation of multivalent Zn^{2+} into/from the cathode is difficult, consequently posing a significant barrier for aqueous ZIBs.[6−9]

Prussian blue analogue (PBA) materials have been explored as cathodes in aqueous ZIBs due to the open framework.[10,11] PBAs, presented as $A_xM[Fe(CN)_6]_y{\cdot}nH_2O$ (where A denotes an alkali/alkaline metal such as K, Na, and Ca and M indicates a transition metal such as Mn, Fe, Cu, Ni, Co, and Zn), have a simple metal cyanide open framework with interstitial ions in the lattice.[12] Liu et al. prepared ZnHCF for aqueous ZIBs showing a high voltage of ∼1.7 V with a capacity of 65.4 mA h g^{-1} at 1 C.[5] However, during galvanostatic cycling, ZnHCF undergoes reversible phase transition and electrochemical decomposition causing capacity fading.[13] N-bonded metal modification can strengthen the structure and enhance the cycling life of PBAs.[14,15] Ni et al. introduced a small amount of Mn ions into N-bonded Zn sites of zinc hexacyanoferrate, and the combination of Mn and Zn in PBAs results in good cycling stability.[13] Adding the suitable metal ions to the electrolyte produces in situ doping effects through the redox reaction to alter dissolution and recombination of the active materials to enhance the electrode stability.[16−18] However, the reactions of Zn metal anodes in the aqueous $ZnSO_4$ electrolyte are complex issues involving zinc anode corrosion, hydrogen evolution, zinc dendrite formation, and alkaline zinc sulfate compromising the performance of ZIBs.[19−23] Hence, a suitable electrolyte containing metal ions and the $ZnSO_4$ electrolyte is crucial.[24] Ni in Ni-based hexacyanoferrate is considered electrochemically inert and can stabilize the structure during redox reactions.[25,26] Zinc−nickel plating on metal anodes has been investigated to enhance the corrosion resistance of Zn anodes,[1] and Ni-containing electrolytes can improve the long-term performance of ZIBs.

In this work, Na-free ZnHCF and Na-rich NaZnHCF cathodes are prepared for aqueous ZIBs. Different concen-

Received: May 11, 2022
Accepted: September 6, 2022
Published: September 16, 2022

tration ratios of $ZnSO_4$ and $NiSO_4$ are investigated, and the ZnHCF cathode shows the best results in the 2 mol L^{-1} $ZnSO_4$ electrolyte with 10 wt % $NiSO_4$ such as a high specific capacity of 71.2 mA h g^{-1} at a current density of 100 mA g^{-1}, a retention of ~93% Coulombic efficiency, a capacity of 58 mA h g^{-1} at 1 A g^{-1}, good rate performance, as well as no obvious attenuation after 150 cycles. The efficient and cost-effective aqueous electrolytes are demonstrated to improve the electrochemical properties for aqueous ZIBs.

2. RESULTS AND DISCUSSION

2.1. Structure and Morphology. Synthesis of ZnHCF and NaZnHCF, as shown in Figure 1a proceeds by simple

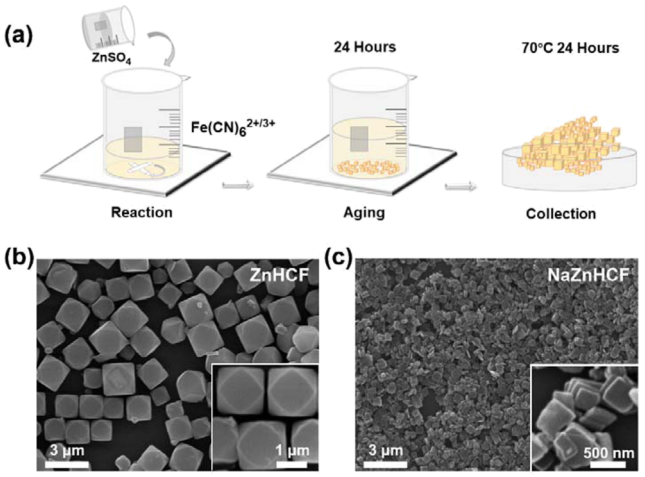

Figure 1. (a) Schematic illustration of the synthesis process and scanning electron microscopy (SEM) images of (b) ZnHCF and (c) NaZnHCF.

coprecipitation without chelator assistance or temperature control. x mmol $ZnSO_4$ was dissolved in 200 mL of H_2O, and y mmol $Fe(CN)_6^{3+/4+}$ was dissolved in 200 mL of H_2O, and then, they were mixed together. The ZnHCF sample with a high crystallinity and regular cut-angle cubic morphology has dimensions ranging from 700 nm to 2 μm (Figure 1b) [x = 2; y = 2; $K_3Fe(CN)_6$]. As shown in Figure 1c, the NaZnHCF sample shows well-defined rhombic nanoplates with an average particle size of 500 nm [x = 2; y = 2; $Na_4Fe(CN)_6$]. The morphology variation is attributed to different concentrations in the solution as shown in Figure S1. A higher concentration leads to faster nucleation, producing irregular particles.[27] Figure S1c shows that ZnHCF has a single-particle morphology when the concentration ratio is small (x/y = 1:1 or 1:2), but at higher concentrations, the particles agglomerate and become irregular. NaZnHCF exhibits a mixed morphology of rhombic particles and nanoplates, and at a high concentration ratio (x/y = 3:2), there are more irregular nanoparticles with different sizes. The different morphologies can be attributed to nucleation and framework evolution at different concentrations.

All the X-ray diffraction (XRD) patterns exhibit sharp and intense peaks, reflecting the crystalline rhombohedral structure,[28] and a larger concentration does not impact the XRD spectra, as shown in Figures S1a,b. The local structures of ZnHCF and NaZnHCF are evaluated by the Rietveld refinement using the GSAS software as shown in Figure 2a,b. The pattern of ZnHCF synthesized without Na ions (Figure

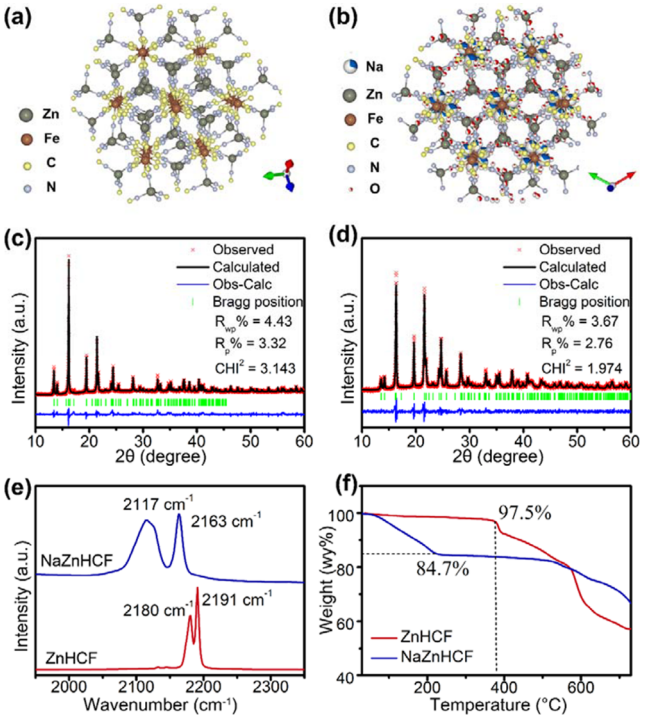

Figure 2. Local structure of (a) ZnHCF and (b) NaZnHCF obtained by the Rietveld refinement using the GSAS software. XRD patterns of (c) ZnHCF and (d) NaZnHCF with the red symbols (×) representing the acquired data, black lines denoting the calculated patterns, light green bars showing the position of Bragg reflections, and blue patterns denoting the difference between the experimental and calculated data. (e) Raman scattering spectra and (f) thermogravimetric analysis (TGA) curves of the as-prepared samples.

2c) shows peaks at 13.42, 14.00, 16.16, 19.46, 21.42, and 21.64°, corresponding to the (104), (110), (113), (024), (116), and (211) planes of the rhombohedral phase $Zn_3[Fe(CN)_6]_2$ (JCPDS no. 38-0688), respectively. The structure belongs to the group of $R\bar{3}c$ with lattice parameters of a = 12.718 Å and c = 32.364 Å.[13] The crystal structure of NaZnHCF synthesized with Na ions (Figure 2d) can be indexed to $Na_2Zn_3[Fe(CN)_6]_2$ (JCPDS no. 36-0539) also with good crystallinity (a = 12.502 Å, c = 32.867 Å, and R_p = 2.76%), showing a rhombohedral structure with the $R\bar{3}c$ space group. Zn-coordinated cyanide changes NaZnHCF/ZnHCF into a different space group known for PBAs which generally have a face-centered cubic structure belonging to the $Fm3m$ space group,[29] in which the FeC_6 octahedra and ZnN_4 tetrahedra are linked by cyanide ligands. The three-dimensional porous structure with large interstitial pores is integrated irregularly with inserted ions and water molecules,[13] which facilitate electrochemical insertion/extraction of different cations including Zn ions *via* a quick and reversible mechanism.[30] ZnHCF provides empty frames, while the NaZnHCF framework is occupied with Na ions and zeolite water due to the charge balance between the initial $Fe(CN)_6^{4-}$ reactants and hydrated Na ions in the precursors.[31]

Raman scattering is performed, and as shown in Figure 2e, the peaks of ZnHCF located at 2180 and 2191 cm^{-1} correspond to the ν(CN) stretching mode of CN− coordinated with Fe(III).[32,33] ν(CN) of NaZnHCF shifts gradually to smaller wavenumbers of 2117 and 2163 cm^{-1}, indicating reduced average valance states of Fe, consistent with

https://doi.org/10.1021/acsomega.2c02930
ACS Omega 2022, 7, 33942−33948

the chemical composition.[34] The FTIR spectrum of ZnHCF in Figure S2 shows bands at 2097 and 2187 cm^{-1} associated with the stretching of cyanide CN.[35] The H−O−H bending mode at 1620 cm^{-1} and O−H stretching at 3617 cm^{-1} of H_2O are not observed, implying negligible water adsorption and coordination in the ZnHCF framework. TGA is performed to determine the water content and material degradation, as shown in Figure 2f. ZnHCF shows a moderate weight loss of ∼2.5 wt % below 380 °C, indicating a small water content. At 400 °C, the weight loss stems from the collapse of the framework.[36] NaZnHCF shows 15.3 wt % weight loss due to adsorption and zeolite water content below 200 °C.[37] NaZnHCF shows a weight loss platform between 200 and 500 °C, indicating better thermal stability than that of sodium-free ZnHCF.[38] The compositions of ZnHCF and NaZnHCF determined by inductively coupled plasma atomic emission spectroscopy (ICP-AES) are listed in Table 1 and the formulas of ZnHCF and NaZnHCF are determined to be $Zn_3[Fe(CN)_6]_2$ and $Na_{1.48}Zn_3[Fe(CN)_6]_{1.824}\cdot 6.18H_2O$ according to ICP and TGA.

Table 1. Composition of ZnHCF and NaZnHCF Determined by ICP-AES

samples	elements	weight (mg kg^{-1})	atomic (mol kg^{-1})
ZnHCF	K	3946.7	0.1
	Zn	408295.9	6.245
	Fe	228159.1	4.085
NaZnHCF	Na	63989.2	2.784
	Zn	368099.5	5.630
	Fe	191168.5	3.423
ZnHCF−$Zn_3[Fe(CN)_6]_2$	NaZnHCF−$Na_{1.48}Zn_3[Fe(CN)_6]_{1.824}\cdot 6.18H2O$		

2.2. Electrochemical Properties. The electrochemical properties are determined at voltages between 0.9 and 1.95 V versus Zn/Zn^{2+} at a constant current of 300 mA g^{-1} in the 2 M $ZnSO_4$ electrolyte as shown in Figure 3. Owing to the narrow stable electrochemical window of the $ZnSO_4$ electrolyte, both

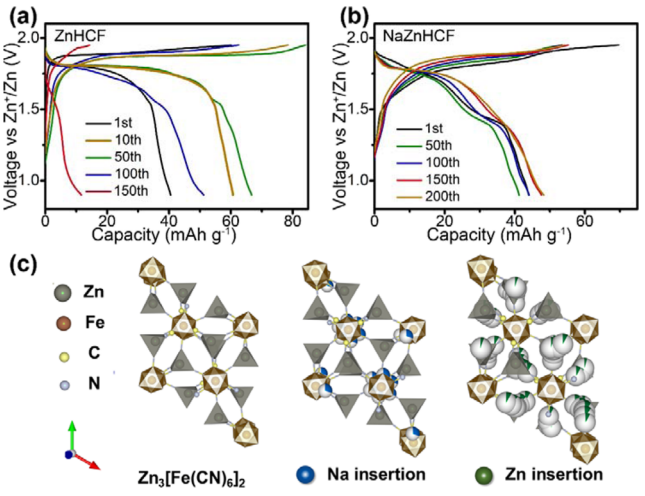

Figure 3. Local charging−discharging curves of (a) ZnHCF and (b) NaZnHCF for different cycles with both samples showing low Coulombic efficiency. (c) Schematic illustration of the primitive cell of $Zn_3[Fe(CN)_6]_2$ with Na/Zn insertion simulated by the GSAS software, the pie charts represent the percentage of occupancy; zinc hexacyanoferrate is present as a trigonal $R\bar{3}c$ phase.

ZnHCF and NaZnHCF have low initial Coulombic efficiencies of 67.4 and 63.1% and first discharging capacities of 40.5 and 43.9 mA h g^{-1}, respectively. During cycling, the discharging capacity of ZnHCF increases rapidly to 60.7 mA h g^{-1} within 10 cycles and then gradually to 66.7 mA h g^{-1} in the following 50 cycles (Figure 3a). The capacity escalation can be ascribed to electrode galvanization in the initial charging−discharging phase.[13] In the following 100 cycles, the Zn storage capacity decreases sharply and is only 11.3 mA h g^{-1} in the 150th cycle. Although dissolution of ZnHCF in the $ZnSO_4$ electrolyte is generally inhibited due to the solubility equilibrium, a small volume of free $[Fe(CN)_6]^{3-}$ may transfer to the anode to cause unsuitable side reactions or recombination with free Zn^{2+} in the electrolyte.[13] NaZnHCF also exhibits a relatively low Coulombic efficiency in the first cycle. The charging and discharging capacities are obviously smaller than those of ZnHCF with a limited discharge capacity of 48.2 mA h g^{-1} (Figure 3b), but there is good consistency after 200 cycles. NaZnHCF contains fewer electrochemically active sites which cause around 20 mA g^{-1} capacity disparity. The standard structure of $Zn_3[Fe(CN)_6]_2$ with Na/Zn insertion is shown in Figure 3c. With regard to ZnHCF, the electrolyte without Ni exhibits higher plateaus at 1.9/1.7 V in the charging/discharging process, respectively, and the low Coulombic efficiency stems from the side reactions.

The electrochemical reactions are monitored in the presence of 10 wt % $NiSO_4$ as shown in Figure 4. For ZnHCF, the

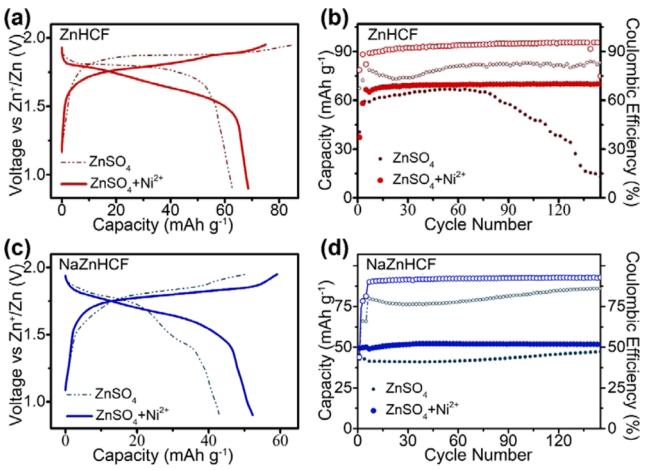

Figure 4. (a,c) Charge−discharge curves of the zinc hexacyanoferrate samples (red for ZnHCF samples and blue for NaZnHCF samples) in a 2 mol L^{-1} $ZnSO_4$ solution (dashed line/small dots) and $ZnSO_4$ solution with 10 wt % $NiSO_4$ (solid line/big dots) at a current density of 300 mA g^{-1}. (b,d) Cyclic stability of zinc hexacyanoferrate samples at a current density of 300 mA g^{-1} (red for ZnHCF samples and blue for NaZnHCF samples; solid dots for specific capacity and hollow circles for Coulombic efficiency). The electrolyte containing Ni ions leads to a better specific capacity, Coulombic efficiency, and cyclic stability.

electrolyte with Ni gives rise to a higher Coulombic efficiency, a larger specific capacity of 69.7 mA h g^{-1} for a current density of 300 mA g^{-1}, and a lower redox potential region from 1.4 to 1.8 V. The capacity increases in the first dozen cycles, and good cyclic stability with 100% capacity retention is observed in the 150th cycle, which is much better than that without Ni. The assembled ZIB exhibits a sudden drop in the following cycles due to battery damage arising from the side reactions in

https://doi.org/10.1021/acsomega.2c02930
ACS Omega 2022, 7, 33942−33948

the R2032 coin cell. As for NaZnHCF, the electrolyte containing Ni yields a higher Coulombic efficiency, a higher specific capacity increase from 42.2 to 51.2 mA h g^{-1}, a long sloping redox platform with a higher average potential, and stable cyclic characteristics. The results confirm that the addition of Ni to the electrolyte improves the specific capacity, Coulombic efficiency, and cycling stability.

To investigate the underlying mechanism, linear sweep voltammetry (LSV) is performed on the Zn metal symmetrical batteries at a scanning rate of 5 mV s^{-1} and a voltage range of 0−2.7 V. Figure 5a shows that in the pure 2 mol L^{-1} $ZnSO_4$

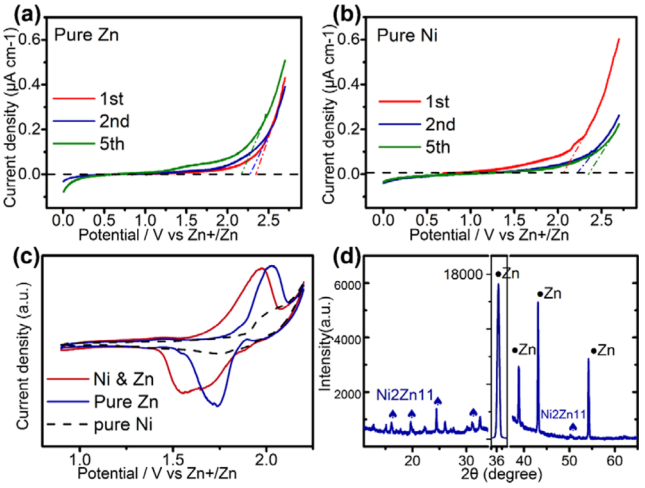

Figure 5. LSV results obtained from the symmetrical cell with Zn metal electrodes in a (a) 2 mol L^{-1} $ZnSO_4$ solution and (b) 1 mol L^{-1} $NiSO_4$ solution. (c) Typical CV curves of the cells with the $Zn_3[Fe(CN)_6]_2$ cathode and Zn metal anode in different electrolytes. (d) XRD pattern of the Zn anode in the hybrid electrolyte containing 2 mol L^{-1} $ZnSO_4$ and 10 wt % $NiSO_4$.

solution, the larger current density in the oxygen evolution reaction (OER) indicates enhanced water splitting due to uneven Zn plating.[39] In the 1 mol L^{-1} $NiSO_4$ solution (Figure 5b), the current density at a high voltage decreases with the number of cycles on account of inhibition of corrosion with the participation of Ni ions.[4] Artificial electrolyte interphase protective layers have been widely applied to protect metal anodes to enhance metal anode stability.[40] The cyclic voltammetry (CV) curves obtained from the cells with the $Zn_3[Fe(CN)_6]_2$ cathode and Zn metal anode in Figure 5c confirm that the redox voltage shifts to a lower potential in the presence of Ni and avoidance of the serious side reaction at a high voltage. There is slight insertion of Ni ions into the $Zn_3[Fe(CN)_6]_2$ cathode. Both Zn^{2+} and Ni^{2+} are inserted into the ZnHCF structure during discharging in the Zn^{2+}/Ni^{2+} solution to increase the capacities. The XRD pattern of the Zn anode in the electrolyte of 2 mol L^{-1} $ZnSO_4$ and 10 wt % $NiSO_4$ after five cycles is shown in Figure 5d, and codeposition of the zinc−nickel alloy is detected to benefit the corrosion resistance of the Zn metal anode in the $ZnSO_4$ solution.[1] As a result, the Ni-assisted redox reaction avoids the serious water splitting side reaction at a high voltage during charging and improves the Zn corrosion resistance during discharging, resulting in an improved electrochemical performance of the Zn hexacyanoferrate cathode and zinc foil anode.

The electrochemical properties of the electrolytes with 2 mol L^{-1} $ZnSO_4$ and different concentrations of $NiSO_4$ (0, 2, 5, 10, and 20 wt %) are shown in Figure 6a. Ni improves the Coulombic efficiency by over 90% and enhances the cyclic

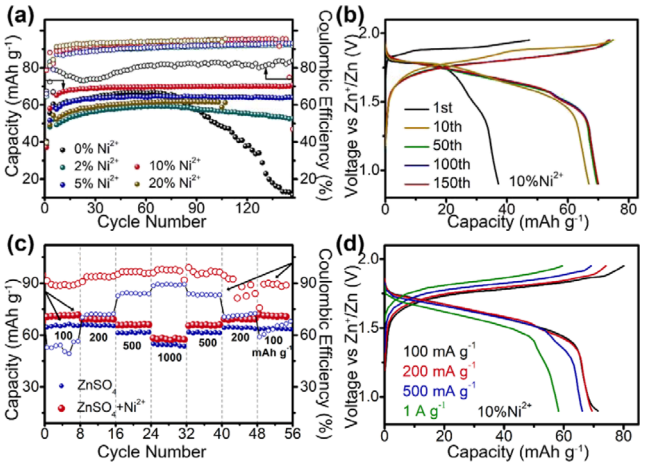

Figure 6. (a) Cyclic characteristics of the ZnHCF cathode and Zn metal anode in electrolytes with different concentrations of $NiSO_4$ at a current density of 300 mA g^{-1}. (Solid dots for specific capacity and hollow circles for Coulombic efficiency.) (b) Charging−discharging curves of the ZnHCF coin cell for different cycles in the electrolyte comprising 2 mol L^{-1} $ZnSO_4$ and 10 wt % $NiSO_4$ showing excellent cycling stability. (c) Rate characteristics of the ZnHCF cathode and Zn metal anode in 2 mol L^{-1} $ZnSO_4$ with (red) and without (blue) 10 wt % $NiSO_4$ (solid dots for specific capacity and hollow circles for Coulombic efficiency). (d) Charging−discharging curves of the ZnHCF coin cell at various rates in the electrolyte with 10 wt % $NiSO_4$.

stability for more than 150 cycles without apparent decay. The electrolyte with 10 wt % $NiSO_4$ yields the highest specific capacity of 71.2 mA h g^{-1}. In each system, Ni gives rise to a capacity increase for 150 cycles, indicating that activation is required to improve the kinetics and discharging capacity.[3] The electrolyte without Ni^{2+} leads to reduced capacities within 150 cycles, and the capacity fades to 0 as shown in Figure 6b in addition to very poor Coulombic efficiency. The 20 wt % Ni^{2+} electrolyte shows a stable capacity of 62 mA h g^{-1} until the 107th cycle, but the cell is damaged afterward.

The rate performance is shown in Figure 6c. Compared to the electrolyte without $NiSO_4$ (blue dots), 2 mol L^{-1} $ZnSO_4$ with 10 wt % $NiSO_4$ (red dots) yields higher average capacities of 71.2, 69.5, 65.8, and 58.2 mA h g^{-1} at current densities of 100, 200, 500, and 1000 mA g^{-1}, respectively. When the current density is reverted back to 100 mA g^{-1}, the reversible capacity recovers to 71 mA h g^{-1}, implying excellent rate capability in the presence of Ni ions in the electrolyte. The charging−discharging curves of ZnHCF at different current densities are shown in Figures 6d and S3. In the presence of 10 wt % $NiSO_4$, the ZnHCF coin cell displays a discharging capacity of 71.2 mA h g^{-1} at a lower current density of 100 mA g^{-1} and a Coulombic efficiency of 90.8% that increases with current densities. The Coulombic efficiency rises to ∼98% at a current density of 1 A g^{-1}. However, without $NiSO_4$, the Coulombic efficiency is only about 60% at low current densities, and serious side reactions occur during the process.

Our study demonstrates that the Ni^{2+}-containing electrolyte (2 mol L^{-1} $ZnSO_4$ + 10 wt % $NiSO_4$) balances Zn loss in the reactions. Both Zn^{2+} and Ni^{2+} are inserted into the ZnHCF structure during discharging in the Zn^{2+}/Ni^{2+} electrolyte,

https://doi.org/10.1021/acsomega.2c02930
ACS Omega 2022, 7, 33942−33948

leading to larger capacities. When Ni^{2+} ions are cointercalated with Zn^{2+} ions during discharging, the deintercalated Ni^{2+} ions dissolve back into the electrolyte and deposit onto the Zn anode during charging. As a result, the reduction/oxidation peaks with shoulders reflect the insertion/extraction processes of both Zn^{2+} and Ni^{2+} cations.

3. CONCLUSIONS

A simple coprecipitation one-step technique is employed to synthesize zinc-based hexacyanoferrate materials for ZIBs. The morphology of the materials is influenced by the concentration of the precursor solution and valence of iron ions. The rhombohedral ZnHCF structure has high crystallinity with diameters ranging from 700 nm to 2 μm. The Na-rich sample, NaZnHCF, consists of rhombic nanoplates with a large number of interstitial water molecules. Both samples have Zn-ion storage capability. ZnHCF has a large capacity of 66.7 mA h g^{-1} but poor cyclic stability as it decomposes during cycling. NaZnHCF shows two zinc-embedding platforms with high cycling stability, but the capacity is only 48.2 mA h g^{-1}. The electrochemical properties of both samples can be enhanced by introducing a small amount of $NiSO_4$ (10 wt %) to the $ZnSO_4$ electrolyte. In the electrolyte containing Ni, the capacity of ZnHCF increases to 71.2 mA h g^{-1} at a current density of 100 mA g^{-1} together with 93% Coulombic efficiency and no noticeable capacity decline after 150 cycles. On the Zn metal anode, codeposition of the zinc−nickel alloy improves the corrosion resistance in the aqueous $ZnSO_4$ electrolyte. The Ni-assisted redox reaction avoids the serious water splitting side reaction at a high voltage during charging, boding well for the Zn corrosion resistance during discharging, leading to an improved electrochemical performance of the Zn hexacyanoferrate cathode and zinc anode systems. This study reveals a promising route to enhance the properties of zinc-based Prussian blue cathodes in aqueous ZIBs by optimizing cost-effective electrolytes.

4. EXPERIMENTAL DETAILS

4.1. Synthesis of ZnHCF and NaZnHCF. The ZnHCF particles were synthesized by a simple coprecipitation technique at room temperature. To prepare solution A, 2 mmol zinc sulfate ($ZnSO_4{\cdot}7H_2O$, Sinopharm Chemical Reagent Co., Ltd, Shanghai, China) was dissolved in 200 mL of deionized water, and 2 mmol potassium ferricyanide ($K_3Fe(CN)_6$, Aladdin Industrial Inc, Shanghai, China) was also dissolved in 200 mL of deionized water to obtain solution B. After vigorous stirring, solution A was added to solution B at ambient temperature. After stirring for a while, the suspension was left to stand for 24 h at room temperature. The sediment was collected by centrifugation, rinsed with deionized water and ethanol twice, and dried at 70 °C for 24 h to obtain cut-angle cubic ZnHCF. The NaZnHCF nanoplates were synthesized by a similar precipitation method, and the only difference was that the hexacyanoferrate source was replaced by $Na_4Fe(CN)_6$.

4.2. Material Characterization. The XRD patterns were obtained using the Panalytical X'pert PRO MRD (Holland) with Cu K_α radiation, and the SEM images were acquired using the TESCAN VEGA3. TGA was performed using the thermogravimetric analyzer, Netzsch STA 449 F3, in an argon atmosphere from room temperature to 800 °C at a heating rate of 10 °C min^{-1}. The Raman scattering spectra were acquired using an Ar ion laser with a wavelength of 532 nm (LabRAM HR800, Horiba, France). The elements were identified by elemental analysis (Vario Micro), and the concentrations of K, Zn, Fe, and Na were determined by ICP-OES (IRIS Intrepid II XSP, Thermo Elemental, USA).

4.3. Electrical Assessment. The working electrodes were designed by mixing the active ingredient (ZnHCF or NaZnHCF), conductive carbon black, and a polytetrafluoroethylene binder with a weight ratio of 7:2:1. The materials were ground using an agate mortar by hand to form a homogeneous mixture, pressed into a thin film, and vacuum-dried at 70 °C for 12 h. Afterward, it was pressed onto a stainless steel mesh (15 μm). The galvanostatic charging−discharging measurements were performed in a regular coin cell (CR2032) consisting of a Zn metal foil (a diameter of 12 mm and a thickness of 30 μm) as the counter electrode and Whatman glass fibers (GF/A, Whatman) as the separator. Five electrolytes containing 2 mol L^{-1} $ZnSO_4$ and different concentrations of $NiSO_4$ (0%, 2%, 5%, 10%, and 20% wt %) were tested. Each cell was prepared under ambient conditions. CV was conducted on an electrochemical workstation (CHI 760E) at 0.1 V s^{-1}, and the galvanostatic charging−discharging experiments were carried out using the battery testing system (Neware BTS 3000n) from 0.9 to 1.95 V (vs Zn/Zn^{2+}) at 25 °C.

■ ASSOCIATED CONTENT

Supporting Information

The Supporting Information is available free of charge at https://pubs.acs.org/doi/10.1021/acsomega.2c02930.

XRD and SEM images of the samples prepared in the different solutions; Fourier transform infrared spectra of ZnHCF and NaZnHCF; charging−discharging curves of ZnHCF at different current densities in the electrolyte without $NiSO_4$; CV curves of the cells with the NaZnHCF cathode and Zn metal anode in different electrolytes; rate characteristics of the NaZnHCF cathode in 2 mol L^{-1} $ZnSO_4$ with 10 wt % $NiSO_4$; and lattice parameters of ZnHCF and NaZnHCF (PDF)

■ AUTHOR INFORMATION

Corresponding Authors

Yue Xu − *School of Materials Science and Engineering and State Key Laboratory for Materials Processing and Die & Mould Technology, Huazhong University of Science and Technology, Wuhan 430074, People's Republic of China; Department of Physics, Department of Materials Science and Engineering, and Department of Biomedical Engineering, City University of Hong Kong, Kowloon 999077 Hong Kong, China*; orcid.org/0000-0002-4677-5173; Email: xuyue@hust.edu.cn

Pei Hu − *School of Science, Hubei University of Technology, Wuhan 430068, People's Republic of China*; Email: hupei@hbut.edu.cn

Authors

Ratul Rehman − *School of Materials Science and Engineering and State Key Laboratory for Materials Processing and Die & Mould Technology, Huazhong University of Science and Technology, Wuhan 430074, People's Republic of China*

Xiaolin Zhang − *Department of Physics, Department of Materials Science and Engineering, and Department of*

https://doi.org/10.1021/acsomega.2c02930
ACS Omega 2022, 7, 33942−33948

Biomedical Engineering, City University of Hong Kong, Kowloon 999077 Hong Kong, China

Miao Chang − *School of Materials Science and Engineering and State Key Laboratory for Materials Processing and Die & Mould Technology, Huazhong University of Science and Technology, Wuhan 430074, People's Republic of China*

Daomin Qin − *School of Materials Science and Engineering and State Key Laboratory for Materials Processing and Die & Mould Technology, Huazhong University of Science and Technology, Wuhan 430074, People's Republic of China*

Yi Liu − *School of Materials Science and Engineering and State Key Laboratory for Materials Processing and Die & Mould Technology, Huazhong University of Science and Technology, Wuhan 430074, People's Republic of China*

Peng Wei − *School of Materials Science and Engineering and State Key Laboratory for Materials Processing and Die & Mould Technology, Huazhong University of Science and Technology, Wuhan 430074, People's Republic of China*

Chao Huang − *Department of Physics, Department of Materials Science and Engineering, and Department of Biomedical Engineering, City University of Hong Kong, Kowloon 999077 Hong Kong, China*

Bin Wang − *Department of Physics, Department of Materials Science and Engineering, and Department of Biomedical Engineering, City University of Hong Kong, Kowloon 999077 Hong Kong, China*

Fangyu Xiong − *Department of Physics, Department of Materials Science and Engineering, and Department of Biomedical Engineering, City University of Hong Kong, Kowloon 999077 Hong Kong, China*

Jiantao Han − *School of Materials Science and Engineering and State Key Laboratory for Materials Processing and Die & Mould Technology, Huazhong University of Science and Technology, Wuhan 430074, People's Republic of China;* orcid.org/0000-0002-9509-3785

Paul K. Chu − *Department of Physics, Department of Materials Science and Engineering, and Department of Biomedical Engineering, City University of Hong Kong, Kowloon 999077 Hong Kong, China;* orcid.org/0000-0002-5581-4883

Complete contact information is available at: https://pubs.acs.org/10.1021/acsomega.2c02930

Author Contributions

‖R.R. and X.Z. contributed equally to this work.

Notes

The authors declare no competing financial interest.

■ ACKNOWLEDGMENTS

This work was supported by the National Natural Science Foundation of China (grant nos. 51902118, 52172201, 51732005, and 52102249), international postdoctoral exchange fellowship program (grant no. PC2021026), China Postdoctoral Science Foundation (grant nos. 2019M662609 and 2020T130217), City University of Hong Kong Strategic Research grant (SRG 7005505), and Shenzhen−Hong Kong Innovative Collaborative Research and Development Program (SGLH20181109110802117 and CityU 9240014).

■ REFERENCES

(1) Chao, D.; Zhou, W.; Xie, F.; Ye, C.; Li, H.; Jaroniec, M.; Qiao, S.-Z. Roadmap for advanced aqueous batteries: From design of materials to applications. *Sci. Adv.* **2020**, *6*, No. eaba4098.

(2) Liu, Z. X.; Huang, Y.; Huang, Y.; Yang, Q.; Li, X. L.; Huang, Z. D.; Zhi, C. Y. Correction: Voltage issue of aqueous rechargeable metal-ion batteries. *Chem. Soc. Rev.* **2020**, *49*, 643−644.

(3) Ming, F.; Liang, H.; Lei, Y.; Kandambeth, S.; Eddaoudi, M.; Alshareef, H. N. Correction to "Layered $Mg_xV_2O_5{\cdot}n\ H_2O$ as Cathode Material for High-Performance Aqueous Zinc Ion Batterie. *ACS Energy Lett.* **2021**, *6*, 2982.

(4) Kundu, D.; Adams, B. D.; Duffort, V.; Vajargah, S. H.; Nazar, L. F. A high-capacity and long-life aqueous rechargeable zinc battery using a metal oxide intercalation cathode. *Nat. Energy* **2016**, *1*, 16119.

(5) Zhang, L. Y.; Chen, L.; Zhou, X. F.; Liu, Z. P. Towards High-Voltage Aqueous Metal-Ion Batteries Beyond 1.5 V: The Zinc/Zinc Hexacyanoferrate System. *Adv. Energy Mater.* **2015**, *5*, 1400930.

(6) Shin, J.; Lee, J.; Park, Y.; Choi, J. W. Aqueous zinc ion batteries: focus on zinc metal anodes. *Chem. Sci.* **2020**, *11*, 2028−2044.

(7) Yang, J. Z.; Yin, B. S.; Sun, Y.; Pan, H. G.; Sun, W. P.; Jia, B. H.; Zhang, S. W.; Ma, T. Y. Zinc Anode for Mild Aqueous Zinc-Ion Batteries: Challenges, Strategies, and Perspectives. *Nano-Micro Lett.* **2022**, *14*, 42.

(8) Huang, M. H.; Mai, Y. J.; Zhao, L. J.; Liang, X. H.; Fang, Z. J.; Jie, X. H. Tuning the kinetics of zinc ion in MoS2 by polyaniline intercalation. *Electrochim. Acta* **2021**, *388*, 138624.

(9) Wang, Z.; Zhou, M.; Qin, L.; Chen, M.; Chen, Z.; Guo, S.; Wang, L.; Fang, G.; Liang, S. Simultaneous regulation of cations and anions in an electrolyte for high-capacity, high-stability aqueous zinc−vanadium batteries. *eScience* **2022**, *2*, 209−218.

(10) Zampardi, G.; Warnecke, M.; Tribbia, M.; Glenneberg, J.; Santos, C.; La Mantia, F. Effect of the reactants concentration on the synthesis and cycle life of copper hexacyanoferrate for aqueous Zn-ion batteries. *Electrochem. Commun.* **2021**, *126*, 107030.

(11) Zampardi, G.; La Mantia, F. Prussian blue analogues as aqueous Zn-ion batteries electrodes: Current challenges and future perspectives. *Curr. Opin. Electrochem.* **2020**, *21*, 84−92.

(12) Li, W. J.; Han, C.; Cheng, G.; Chou, S. L.; Liu, H. K.; Dou, S. X. Chemical Properties, Structural Properties, and Energy Storage Applications of Prussian Blue Analogues. *Small* **2019**, *15*, 1900470.

(13) Ni, G.; Xu, X. W.; Hao, Z.; Wang, W. W.; Li, C. Y.; Yang, Y. X.; Zhou, C. G.; Qin, L.; Chen, W. C.; Yao, X.; Cai, J. Tuning the Electrochemical Stability of Zinc Hexacyanoferrate through Manganese Substitution for Aqueous Zinc-Ion Batteries. *ACS Appl. Energy Mater.* **2021**, *4*, 602−610.

(14) Qiu, Y.; Lin, Y.; Yang, H. B.; Wang, L. Ni-doped cobalt hexacyanoferrate microcubes as battery-type electrodes for aqueous electrolyte-based electrochemical supercapacitors. *J. Alloys Compd.* **2019**, *806*, 1315−1322.

(15) Huang, B.; Shao, Y. J.; Liu, Y. C.; Lu, Z. Y.; Lu, X. Y.; Liao, S. J. Improving Potassium-Ion Batteries by Optimizing the Composition of Prussian Blue Cathode. *ACS Appl. Energy Mater.* **2019**, *2*, 6528−6535.

(16) Zhang, N.; Cheng, F. Y.; Liu, J. X.; Wang, L. B.; Long, X. H.; Liu, X. S.; Li, F. J.; Chen, J. Rechargeable aqueous zinc-manganese dioxide batteries with high energy and power densities. *Nat. Commun.* **2017**, *8*, 405.

(17) Zhong, C.; Liu, B.; Ding, J.; Liu, X.; Zhong, Y.; Li, Y.; Sun, C.; Han, X.; Deng, Y.; Zhao, N.; Hu, W. Decoupling electrolytes towards stable and high-energy rechargeable aqueous zinc−manganese dioxide batteries. *Nat. Energy* **2020**, *5*, 440−449.

(18) Huang, M.; Meng, J.; Huang, Z.; Wang, X.; Mai, L. Ultrafast cation insertion-selected zinc hexacyanoferrate for 1.9 V K−Zn hybrid aqueous batteries. *J. Mater. Chem. A* **2020**, *8*, 6631−6637.

(19) Dunn, B.; Kamath, H.; Tarascon, J. M. Electrical Energy Storage for the Grid: A Battery of Choices. *Science* **2011**, *334*, 928−935.

(20) Zhang, Y. J.; Wang, Y.; Lu, L.; Sun, C. W.; Yu, D. Y. W. Vanadium hexacyanoferrate with two redox active sites as cathode

material for aqueous Zn-ion batteries. *J. Power Sources* **2021**, *484*, 229263.
(21) Zhang, B. Y.; Qin, L. P.; Fang, Y.; Chai, Y. Z.; Xie, X. S.; Lu, B. A.; Liang, S. Q.; Zhou, J. Tuning Zn2+ coordination tunnel by hierarchical gel electrolyte for dendrite-free zinc anode. *Sci. Bull.* **2022**, *67*, 955−962.
(22) Liu, Z. X.; Qin, L. P.; Lu, B. A.; Wu, X. W.; Liang, S. Q.; Zhou, J. Issues and Opportunities Facing Aqueous Mn2+/MnO2-based Batteries. *Chemsuschem* **2022**, *15*, No. e202200348.
(23) Cao, J.; Zhang, D.; Chanajaree, R.; Yue, Y.; Zeng, Z.; Zhang, X.; Qin, J. Stabilizing zinc anode via a chelation and desolvation electrolyte additive. *Adv. Powder Mater.* **2022**, *1*, 100007.
(24) Nie, X. Y.; Miao, L. C.; Yuan, W. T.; Ma, G. Q.; Di, S. L.; Wang, Y. Y.; Shen, S. G.; Zhang, N. Cholinium Cations Enable Highly Compact and Dendrite-Free Zn Metal Anodes in Aqueous Electrolytes. *Adv. Funct. Mater.* **2022**, *32*, 2203905.
(25) Li, J. L.; Du, Z. J.; Ruther, R. E.; An, S. J.; David, L. A.; Hays, K.; Wood, M.; Phillip, N. D.; Sheng, Y. P.; Mao, C. Y.; Kalnaus, S.; Daniel, C.; Wood, D. L. Toward Low-Cost, High-Energy Density, and High-Power Density Lithium-Ion Batteries. *JOM* **2017**, *69*, 1484−1496.
(26) Bin, D.; Wen, Y. P.; Wang, Y. G.; Xia, Y. Y. The development in aqueous lithium-ion batteries. *J. Energy Chem.* **2018**, *27*, 1521−1535.
(27) Yue, Y. F.; Binder, A. J.; Guo, B. K.; Zhang, Z. Y.; Qiao, Z. A.; Tian, C. C.; Dai, S. Mesoporous Prussian Blue Analogues: Template-Free Synthesis and Sodium-Ion Battery Applications. *Angew. Chem., Int. Ed.* **2014**, *53*, 3134−3137.
(28) Zhang, L. Y.; Chen, L.; Zhou, X. F.; Liu, Z. P. Morphology-Dependent Electrochemical Performance of Zinc Hexacyanoferrate Cathode for Zinc-Ion Battery. *Sci. Rep.* **2015**, *5*, 18263.
(29) Lee, H.; Kim, Y. I.; Park, J. K.; Choi, J. W. Sodium zinc hexacyanoferrate with a well-defined open framework as a positive electrode for sodium ion batteries. *Chem. Commun.* **2012**, *48*, 8416−8418.
(30) Ma, L. T.; Chen, S. M.; Long, C. B.; Li, X. L.; Zhao, Y. W.; Liu, Z. X.; Huang, Z. D.; Dong, B. B.; Zapien, J. A.; Zhi, C. Y. Achieving High-Voltage and High-Capacity Aqueous Rechargeable Zinc Ion Battery by Incorporating Two-Species Redox Reaction. *Adv. Energy Mater.* **2019**, *9*, 1902446.
(31) Tirler, A. O.; Persson, I.; Hofer, T. S.; Rode, B. M. Is the hexacyanoferrate (II) anion stable in aqueous solution? A combined theoretical and experimental study. *Inorg. Chem.* **2015**, *54*, 10335−10341.
(32) Hadjiivanov, K. I.; Panayotov, D. A.; Mihaylov, M. Y.; Ivanova, E. Z.; Chakarova, K. K.; Andonova, S. M.; Drenchev, N. L. Power of Infrared and Raman Spectroscopies to Characterize Metal-Organic Frameworks and Investigate Their Interaction with Guest Molecules. *Chem. Rev.* **2021**, *121*, 1286−1424.
(33) Silva, M. N. T.; Ardisson, J. D.; Fabris, J. D.; Nossol, E. Zinc Hexacyanoferrate/Multi-Walled Carbon Nanotubes Films for Rechargeable Aqueous Batteries. *J. Braz. Chem. Soc.* **2020**, *31*, 1787−1795.
(34) You, Y.; Yu, X. Q.; Yin, Y. X.; Nam, K. W.; Guo, Y. G. Sodium iron hexacyanoferrate with high Na content as a Na-rich cathode material for Na-ion batteries. *Nano Res.* **2015**, *8*, 117−128.
(35) Rodríguez-Hernández, J.; Reguera, E.; Lima, E.; Balmaseda, J.; Martínez-García, R.; Yee-Madeira, H. An atypical coordination in hexacyanometallates: Structure and properties of hexagonal zinc phases. *J. Phys. Chem. Solids* **2007**, *68*, 1630−1642.
(36) Min, X.; Xiao, J.; Fang, M. H.; Wang, W.; Zhao, Y. J.; Liu, Y. G.; Abdelkader, A. M.; Xi, K.; Kumar, R. V.; Huang, Z. H. Potassium-ion batteries: outlook on present and future technologies. *Energy Environ. Sci.* **2021**, *14*, 2186−2243.
(37) Lai, J.; Zhu, H.; Zhu, X.; Koritala, H.; Wang, Y. Interlayer-Expanded V6O13·nH2O Architecture Constructed for an Advanced Rechargeable Aqueous Zinc-Ion Battery. *ACS Appl. Energy Mater.* **2019**, *2*, 1988−1996.
(38) Chen, Y. C.; Woo, H. J.; Rizwan, M.; Yahya, R. B.; Cui, D. H.; Luo, D.; Chen, L.; Arof, A. K. M.; Wang, F. Nanoscale Morphology Control of Na-Rich Prussian Blue Cathode Materials for Sodium Ion Batteries with Good Thermal Stability. *ACS Appl. Energy Mater.* **2019**, *2*, 8570−8579.
(39) Yang, Y.; Tang, Y.; Fang, G.; Shan, L.; Guo, J.; Zhang, W.; Wang, C.; Wang, L.; Zhou, J.; Liang, S. Li+ intercalated V2O5·nH2O with enlarged layer spacing and fast ion diffusion as an aqueous zinc-ion battery cathode. *Energy Environ. Sci.* **2018**, *11*, 3157−3162.
(40) Lu, W.; Sun, L.; Zhao, Y.; Wu, T.; Cong, L.; Liu, J.; Liu, Y.; Xie, H. Elongating the cycle life of lithium metal batteries in carbonate electrolyte with gradient solid electrolyte interphase layer. *Energy Storage Mater.* **2021**, *34*, 241−249.

https://doi.org/10.1021/acsomega.2c02930
ACS Omega 2022, 7, 33942−33948